Evaluation of Acoustic Propagation in Layered Media using Wave Confinement

Subhashini Chitta
Wave CPC, Inc
Tullahoma, TN

Mary L. Houston
Analytical Mechanics Associates, Inc.
Hampton, VA, USA

James H. Stephenson
U.S. Army Combat Capabilities Development Command Aviation & Missile Center
Hampton, VA, USA

John Steinhoff
Wave CPC, Inc
Tullahoma, TN

ABSTRACT

A comprehensive method for propagation of sound in layered media is discussed that involves dividing the domain into two regions, source field and far field. The source field is provided using experimentally collected data from full-scale rotorcraft acoustic flight tests, which consists of short waveforms that cannot be directly simulated on the grid without numerical errors. Instead, grid-based computational waves are used to carry the details of these waveforms, including amplitude, arrival time and location of origin on source sphere. This is done by solving the scalar wave equation using the Wave Confinement (WC) method, which involves adding an extra term to produce converged solutions. WC is used to study wave propagation in two different atmospheric conditions, and the results are compared to the flight test data. Overall, WC can accurately capture the propagation effects, and there is good agreement with the flight test data.

INTRODUCTION

Wave propagation modeling in layered media has become increasingly important since it is applicable to a wide range of physical problems such as sound propagation through the atmosphere, seismic wave propagation through layered soils, radio wave propagation through layered ionosphere, etc. (Refs. 1, 2). Within the first category is long range rotorcraft noise propagation in realistic environments, which is the application of interest for this paper.

The acoustic emissions from rotorcraft vehicles is of critical concern to the design of new aircraft, such as those in development for Urban Air Mobility (UAM) applications (Refs. 3–6). Once new rotorcraft are produced, they go through acoustic emissions testing to capture the acoustic emissions of the vehicles under a variety of flight conditions (Ref. 7). This information is then used to assess whether the new vehicle conforms to acoustic performance and certification requirements, and to also provide the basis for land-use modeling and inform community noise reduction for the vehicle in flight (Ref. 8).

In order to model rotorcraft-induced community noise, not only do the rotorcraft acoustic emissions have to be modeled correctly, but also the propagation of those emissions must be captured with high fidelity. The main factors that significantly affect propagation are geometric spreading, atmospheric absorption, ground or surface reflections, ground impedance, refraction, and diffraction.

This paper focuses on refraction, which is caused by varying atmospheric conditions, most importantly temperature and wind gradients, as a function of the vertical coordinate, z. In a homogenous medium (for instance, an atmosphere with calm winds and no temperature gradient), propagation follows straight lines indefinitely. An example of a point source propagating as a spherical wave in a homogeneous medium is shown in Figure 1. In such a medium, geometric spreading will result in a $1/r$ loss, where r is the radius of curvature of the 'ray tube' and increases linearly with distance from the source.

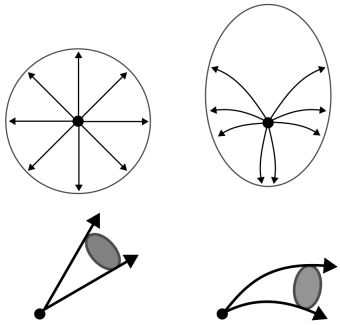

Figure 1: Top: Snapshots of a wavefront with rays pointing in the direction of propagation with homogenous medium on the left and stratified medium on the right. Below: Ray tube demonstration for straight and curved rays.

In a layered medium, the speed of sound, c, is not constant, and the waves do not propagate in straight lines. Therefore, the shape of the wave changes during propagation, and r does not necessarily increase linearly with distance from the source, which can be seen in Figure 1. In an inhomogeneous medium, r can also decrease; when atmospheric conditions, specifically temperature and wind gradients, result in converging rays, the radius of the 'ray tube' decreases, causing the sound to be louder than expected at certain receiver locations. In the same way, temperature or wind gradients can cause the waves to diverge at a faster rate, resulting in formation of qui-

Presented at the Vertical Flight Society's 79th Annual Forum & Technology Display, West Palm Beach, FL, USA, May 16–18, 2023.

eter than expected regions. In this paper, recent advances in modeling sound propagation in inhomogeneous media using Wave Confinement (WC) (Ref. 9) will be presented.

For long distance propagation of relatively short waves, attempting to accurately solve the detailed propagation equations is not feasible due to numerical dissipation. Instead, Wave Confinement captures the acoustic fields using stable, self-confining solitary waves, which are defined by eigenfunctions associated with isolated eigenvalues. This is achieved by adding an eigenfunction operator to the propagation equation to eliminate numerical dissipation while conserving the essential dynamics. The modified equations are then discretized using lower order methods for computational simulations. This feature assures their stability in the presence of discretization error.

A comprehensive analysis of rotorcraft noise propagation involves source modeling and far field propagation. Although far field propagation is not affected by the errors in source models, these errors will be carried over into the final solutions. Therefore, a reasonably accurate source model is needed for better prediction of far field rotorcraft noise. Typically, source hemispheres are measured by flying a vehicle in steady state over a linear array of microphones. As the vehicle passes over the array of microphones, acoustic data are measured for different presentation angles. This allows for a vehicle-centered noise hemisphere to be constructed (Ref. 10), assuming steady level flight is maintained.

SOURCE MODELING

The source models for this paper take the form of an acoustic hemisphere generated from flight test experimental data. The data were collected in Yuma, Arizona, using an MD530 rotorcraft as the noise source. Sixty-three GRAS 67AX microphones were deployed and sampled simultaneously throughout each run at 25 kHz with 24-bit resolution. The microphones have a 0.5 inch diaphragm and are flush-mounted on an acoustically hard ground board measuring 15 inches in diameter. To minimize edge effects, the microphones are mounted off-center on the ground boards, in accordance with SAE Aerospace Recommended Practice ARP4055 (Ref. 11). The microphone array layout can be seen in Figure 2. A Cartesian coordinate system is used to describe the location of the microphones with respect to the flight path. The coordinate x is defined along the flight track and is positive in the primary flight direction; y is defined perpendicular to the flight track and is positive to the aircraft left side; z is above the ground. Microphones were generally numbered sequentially from the negative to positive in the 'x' direction, and from positive to negative in the 'y' direction, with microphone 31 at (0,0,0). The details of the experimental setup and procedures are well documented in Refs. 12 and 13.

The microphone array was, in fact, composed of four interlaced arrays; one linear array and three snapshot arrays. The linear array initially consisted of 13 microphones along the y-axis at x = 0. Ultimately, additional microphones located

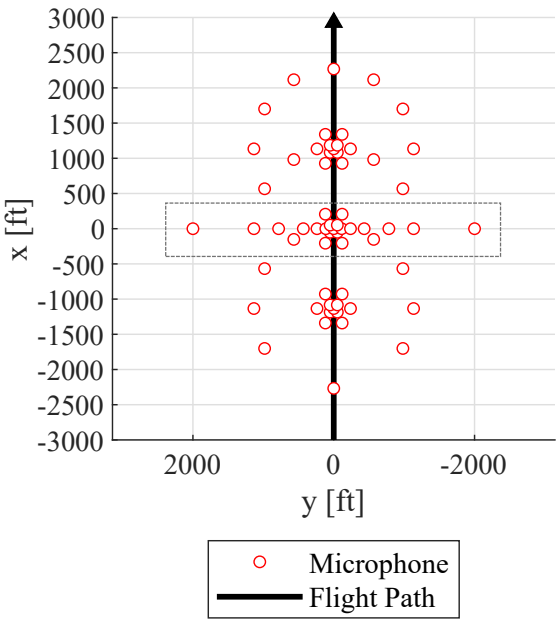

Figure 2: Microphone locations for test site array. Microphones used to generated the noise hemisphere enclosed by dashed line.

a short distance before and after the linear array were included to provide better coverage below the vehicle. These are enclosed by the dashed line in Figure 2. As the rotorcraft passes over the linear array, the microphones sample continuously, and a spectrum can be calculated every 0.5s, capturing a range of presentation angles. This allows the array to effectively have many times more microphones than were physically deployed. This method requires that the pilot maintain a steady flight condition, as the vehicle must be in the same aerodynamic state for the duration of the flyover to allow acoustic measurements taken at different points in time to be mapped back to the same hemisphere. The snapshot arrays were used to investigate instantaneous acoustic measurements, which will not be addressed in the current paper. Details of which can be found in Refs. 12 and 13.

Regardless of the array used, the acoustic signal is de-Dopplerized in the time domain using the methodology described in Ref. 14. De-Dopplerization is needed to correct the variation in frequency shift as the vehicle passes over the array. The de-Dopplerized signal is then transformed into narrowband spectral form (dB, Reference atmosphere of 20 μPa, 4Hz bin width) and backpropagated from the microphones to the vehicle to form a source hemisphere of 100-foot radius. Narrowband spectra were chosen to resolve the lower frequencies, especially, main and tail rotor blade passage frequencies and harmonics that are more relevant to long distance propagation (Ref. 15). Pressure-time data are divided into 0.5s increments, with three transforms taken from the first, second and middle 0.25s of the increment and averaged. The spectra are calculated using Welch's power spectral method from a Hamming window. The resulting spectra are converted from power spectral densities to sound pressure levels by correcting for the bin width ($+10\ \log_{10}(\Delta f)$).

Factors that would have affected the acoustic signal as it traveled from the vehicle to the microphones, such as atmospheric absorption and perfectly reflecting ground, are accounted for in this process. Also, the atmosphere is assumed to be homogenous and straight ray propagation is used. Therefore, geometric attenuation is modeled as spherical spreading, which reduces the amplitude of all frequencies equally. Atmospheric absorption is accounted for as a function of temperature, relative humidity and atmospheric pressure, with high frequencies being more effected than low frequencies (Refs. 16–18). Because acoustically hard ground boards were used, ground effects were accounted for through simple pressure doubling (Ref. 19). The shorter distances used in the creation of source hemisphere (on the order of one thousand feet instead of several thousand feet) limit the effects of atmospheric conditions on propagation, making the straight ray propagation method an acceptable choice. What cannot be accounted for in this method of source modeling are the effects that atmospheric conditions have on the source noise production mechanisms, the impacts of which are discussed later.

A Lambert projection of coverage by the linear array for a 120 kts steady level flight can be seen in Figure 3, where the black points represent mapped microphone locations. The Lambert projection represented the hemisphere in azimuth and elevation angles, denoted as ψ and α, respectively. Azimuth is measured from 0° to 360°, with 180° at the nose and 0° at the tail. By convention, the direction of azimuth is defined to be with the rotation of the main rotor, which is counter clockwise for the MD530 rotorcraft. Therefore 90° is on the right side of the vehicle where the blade is advancing, and 270° is on the left side where the blade is retreating. When the vehicle is on the flight track, its nose is pointing in the positive x-direction, and the right side is toward the negative y-direction. Elevation angle is defined such that 0° is at the horizon and $-90°$ is directly below the vehicle. It can be seen that the microphone coverage on the hemisphere is uneven, with more data near the horizon plane than beneath the vehicle. To obtain even coverage on the source hemisphere, an inverse distance weighting scheme is used to interpolate the data onto a uniform grid. Details of the interpolation method will be discussed later.

FAR FIELD PROPAGATION

There are a number of grid-based methods that have been developed for long-distance wave propagation. These include finite difference time domain (FDTD) methods, parabolic equation (PE) methods, and Green's functions, among others.

Conventional FDTD approaches solve the wave equation by formulating governing partial differential equations, applying higher-order discretizations, and solving them as accurately as possible on feasible computational grids, assuming smooth enough solutions. The successful application of these is limited by the requirement that a sufficient number of grid cells must span the wave to accurately solve the equations, and that the propagation distance is not too long compared to the wavelength (Refs. 20–22). Due to numerical dissipation, conventional higher-order methods may not be feasible for thin

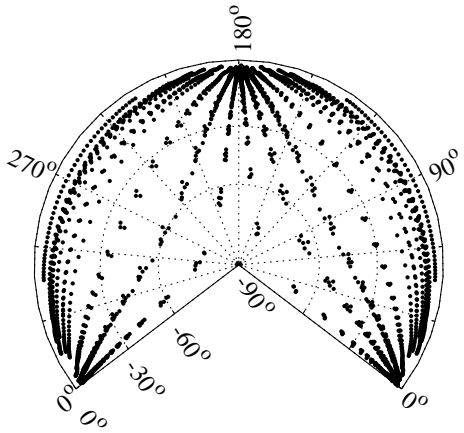

Figure 3: Microphones projected from linear array onto noise source hemisphere.

waves propagating over long distances.

In a few cases, better accuracy can be provided using parabolic equation methods, which are approximations of Helmholtz equations. However, these methods are typically limited to two dimensions, based on axisymmetric approximations, neglecting contributions from larger elevation angles (Ref. 23). Later, Wide Angle Parabolic Equation (WAPE) approximations (Refs. 24, 25) were introduced to account for larger angles, but these involve computationally expensive LU decomposition methods and are limited to flat and hard grounds where an image source is used to account for reflections. Also, the marching step size for WAPE approximations is dependent on the wavelength of the signal.

To reduce the computing time, the Green's function Parabolic Equation (GFPE) method was developed, which uses forward and inverse Fourier transforms (Refs. 26, 27). One of the advantages of the GFPE method is the use of larger marching steps, which is a significant factor in reducing the computational time. However, the accuracy of the GFPE method is limited by the starting field (or the initial condition), which needs to be rederived for every atmospheric and ground condition (Ref. 23).

Another approximation that is well-known for fast computation is ray tracing, which is a Lagrangian formulation. This involves solving a set of ordinary differential equations to follow discrete rays that are normal to the wavefront and obey Snell's Law. When the number of rays are infinitely large, they can represent a surface with constant phase. While ray tracing can provide reasonably accurate qualitative insight, there are several drawbacks that can make it unsuitable for propagation in realistic environments. One of them involves interpolation to compute atmospheric and ground variables at each ray location. Also, in nonhomogeneous media, rays are not uniformly distributed during propagation. For example, regions with diverging rays will cause the wavefront to be poorly sampled, and therefore, new rays need to be introduced by interpolation (Ref. 28). It is important to note that any small perturbation during these interpolations will grow over long distances, significantly effecting the accuracy. Another significant drawback is the difficulty in calculating the

amplitude when atmospheric variations are present and rays do not propagate in straight lines. In general, the amplitude is calculated as $1/r$, where r is the radius of curvature of the ray tube. In a homogeneous medium, r is equal to the path length, l. When rays are curved, $r \neq l$, and is calculated using the normal distance between rays, which requires more interpolation.

Taking all the above limitations into account, a grid-based method, Wave Confinement, is described, which involves simpler equations (even in 3-D) and does not incur numerical dissipation. One of the advantages of WC is the use of solitary waves to represent the physical waveform on the grid and propagate it indefinitely (Ref. 9). For long distance propagation, attempting to accurately solve the detailed structure of physical waves is computationally prohibitive. Instead, a dynamic surface extension will extend the source surface into the far field without information loss due to numerical error, as well as preserve the shape of the physical waveform despite the use of coarse grids. In contrast to Lagrangian ray tracing, WC is an Eulerian-based method that captures the waves directly on the computational grid, where the solutions are codimension 1 surfaces (in the fine grid limit), defined on a regular grid, rather than collections of rays. Also, unlike ray tracing schemes, which suffer from scarcity of grid nodes in the far field, WC can still capture waves as smooth surfaces without complex logic involving continual addition of new rays through interpolation.

Wave Confinement Description

In this paper, we consider the following three-dimensional scalar wave equation,

$$\partial_t^2 \phi = c^2 \nabla^2 \phi, \tag{1}$$

where ϕ represents the physical waveform on the grid and c is the speed of sound. Dissipative and dispersive errors are introduced when Equation (1) is discretized using conventional Taylor expansion-based schemes. It is possible to eliminate this behavior by extending the wave equation with the addition of an extra term. The modified wave equation will then be,

$$\partial_t^2 \phi = c^2 \nabla^2 \phi + \partial_t \nabla^2 F, \tag{2}$$

where F is a nonlinear function of ϕ. Within the frame of the solution, a type of diffusion and anti-diffusion are maintained in a state of nonlinear equilibrium to converge the solution toward a target eigenfunction. While the detailed description of this process is beyond the scope of this paper, it is important to note that this eigenfunction has the same characteristics as a solitary wave, which also exists due to the presence of opposing fields, diffusion and anti-diffusion, and stays thin over indefinitely long times. Also, despite the added term, the "modified" wave equation also has rotational and translational invariances, conserving the essential integrals, such as the amplitude, propagation velocity, and arrival time. More details of the eigenfunction are discussed in Ref. 9.

Wave Confinement precludes conventional resolution of the physical waveform, but it permits the determination of a set of variables such as emission coordinates and integrated amplitude and arrival time of the physical waves over the entire spatial and temporal domain of interest. These variables are then used to "reconstruct" an accurate approximation of the physical waveform in localized areas of interest, which are carried by a multicomponent computational wave, ϕ_k, propagated over the entire domain. Although initial condition can be arbitrary, it relaxes to the form,

$$\phi_k = l_k \operatorname{sech}\left[\gamma(\bar{r} - R_{cw})\right], \tag{3}$$

where $\bar{r}$ is the distance from the source and R_{cw} is the radius of the surface, where the computational waves are initialized. γ is the thickness factor of the computational waves, k is the index of the component, and $l_k = (1, x, y, z)$ for $k = 1, 2, 3, 4$, respectively. γ is independent of the grid cell size, determines the number of grid points across the wave, and is not a function of the physical wavelength. The radius of the source sphere in grid units, R_{grid}, needs to be at least 6.5, while the number of grid points between the source and ground (N_s, shown in Figure 4) is chosen such that the entire initial computational wave is above the ground. N_s must be at least 15 grid units, so the maximum grid cell size around the source is limited to $ds = \frac{z_s}{15}$, where z_s is the source height. For uniform grid, this is the maximum grid cell size for the entire domain.

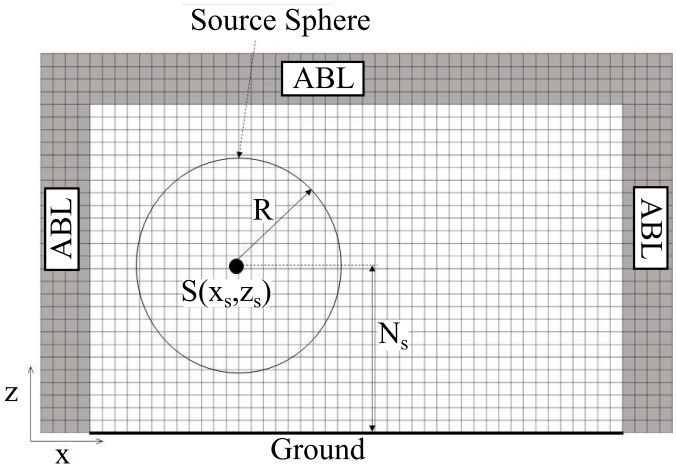

Figure 4: Computational domain in xz plane with Absorbing Boundary Layers (ABL). Source is located at x_s, z_s, with source sphere radius in ft, R

To maintain rotational invariance and translational invariance, the modified wave equation is discretized only using second-order central differences. This discretized equation (like Equation (1)) will accommodate all linear propagation effects such as reflections, refraction due to temperature gradients, and diffraction. To include the effects due to nonzero background wind, ($\vec{u} \neq 0$), an additional equation,

$$\frac{\partial \phi_k}{\partial t} = -\vec{u} \bullet \nabla \phi_k \tag{4}$$

is solved every time-step. The variations in wind speed are only assumed to be in x and y directions. Therefore, $\vec{u} = (u_x, u_y)$, where u_x and u_y are the x and y components, respectively.

The numerical solution of the time dependent wave equation also requires the implementation of an artificial absorbing boundary to represent open boundaries. This artificial boundary comprises a few layers surrounding the computational domain as shown in Figure 4, where a multidimensional advection equation,

$$\frac{\partial \phi_k}{\partial t} = -c\hat{n} \bullet \nabla \phi_k \tag{5}$$

is solved. $\hat{n}$ is the normal vector computed as

$$\hat{n} = (\frac{x - x_s}{\bar{r}}, \frac{y - y_s}{\bar{r}}, \frac{z - z_s}{\bar{r}}), \tag{6}$$

where x_s and y_s are the x and y coordinates of the source, respectively. This is similar to Ref. 29, where 1-D advection, $\hat{n} = (1,0,0)$, is used at the left boundary.

As the computational wave passes a grid point, arrival time (τ), geometric attenuation factor (A_f), and emission angles (elevation (α_{emit}), azimuth (ψ_{emit})) are calculated. These will be used later to predict sound spectra at specified microphone locations.

Validation

WC has already been demonstrated to accurately capture wave bending due to temperature and wind gradients separately in Ref. 30. In this section, combined effects due to wind and temperature are shown using WC. In general, the atmospheric variations are only assumed to be in the z direction and that the propagation is approximately axisymmetric, which is the premise of many sound propagation methods. This is not true since the presence of wind can affect the propagation as a function of azimuth as well, despite the variation only in the z-direction. Since the WC method computes the propagation of the entire wavefront, azimuth dependent effects can also be accurately captured, as shown later.

Propagation is also affected by the source height, especially when there is varying temperature and wind. The flight test data provided for this analysis were collected for altitudes of $\sim$150 ft above ground level. However, for this validation section, a larger source height is used to allow a coarser grid. Further, the functional form of the temperature and wind data are chosen to allow the source to stay within the atmospheric boundary, where wind variations are nonzero, as shown in Figure 5. Since the restriction on grid cell size is more due to source position than the atmospheric gradients, coarser grids can be used, while still permitting the specification of varying atmospheric and topographic features.

For any wind blowing from an angle, β, $\vec{u}$ in Cartesian coordinates is calculated as

$$\vec{u} = (u\cos(\beta), u\sin(\beta)). \tag{7}$$

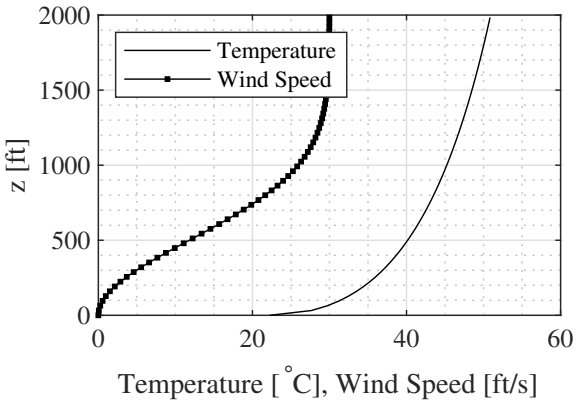

Figure 5: Temperature and wind profile as a function of height for validation study.

A headwind is defined as wind blowing from $\psi = 180°$, such that $\beta = 180°$ and $\vec{u} = (u_x < 0, u_y = 0)$. Crosswind is defined as wind blowing from $\psi = 90°$, such that $\beta = 90°$ and $\vec{u} = (0, u_y > 0)$.

For the first validation, a tailwind is assumed, which is blowing from $\psi = 0°$ ($\beta = 0°$) and therefore, $\vec{u} = (u_x > 0, 0)$. The source is located at $(0,0,714$ ft) above the ground, which allows a maximum grid cell size of 32 ft on a uniform grid. Equations (2) and (4) are then solved with initial and boundary conditions discussed in the previous section.

At $\psi = 180°$, the wind is blowing in the same direction as the wave normal (or direction of propagation), resulting in downward bending. At $\psi = 0°$, the wind is blowing in the direction opposite to the wave normal, which refracts the waves upward. This behavior is shown in Figure 6a, where elevation contours are expanding in the $\psi = 0°$ direction, and contracting in $\psi = 180°$ direction. Rays in specific azimuth planes are also deployed to compare with WC computation. It can be seen that the angles above the horizon reach the ground due to downward bending.

It is known that azimuth angles do not deviate significantly unless there are significant crosswind speeds in excess of 100 kts (Ref. 31). Therefore, along the direction of propagation, ψ_{emit} should be constant. This is verified for both WC and ray tracing solutions in Figure 6b, where a computation for homogeneous medium (dashed lines) is also plotted. Although the deviation in azimuth angle itself is negligible, the amount of bending depends on $\psi - \beta$. This means that the propagation is not axisymmetric, and so a full three-dimensional solution is required for this and similar cases.

Another variable that can significantly vary due to refraction is geometric attenuation, which is demonstrated using the dBLoss, calculated as

$$dBLoss = 20\log_{10}(A_f). \tag{8}$$

Since $A_f = \frac{1}{r}$ and r is always positive, then A_f is always less than 1 for a point source, and dBLoss will always be negative. This means, for a source of 100 dB, if the dBLoss is -40 dB at a point, then the corresponding sound amplitude at that location is 60 dB. The reason to choose this variable is

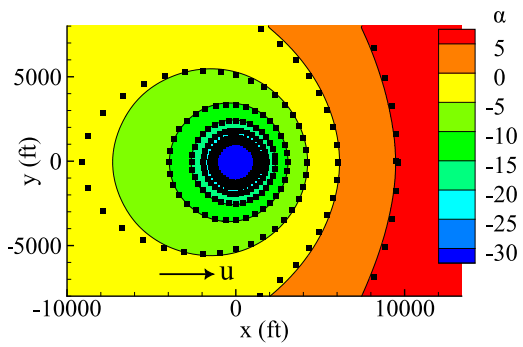

(a) Elevation angles (α_{emit}) on ground computed using WC (in color) compared with ray tracing (filled squares).

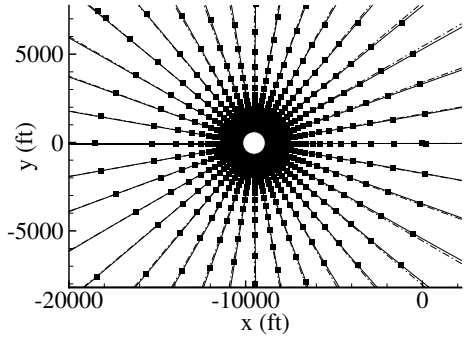

(b) Azimuth angles (ψ_{emit}) computed using WC (solid line) compared with homogeneous medium (dashed line) and ray tracing (filled squares).

Figure 6: Emission angles on ground for the medium in Figure 5 with wind blowing from $\psi = 0°$ (toward positive x direction).

that it is independent of the source strength and will be the same for a given atmospheric condition. Like elevation angles, the amount of attenuation (or dBLoss) depends on the angle difference, $\psi - \beta$. When $\psi - \beta = 0°$, the wind is blowing opposite to the direction of propagation, resulting in small attenuation levels and thus a louder signal. This can be seen in Figure 7 for $\beta = 0°$, where the the sound signal at the ground is stronger in the front ($\psi = 180°$, +x direction).

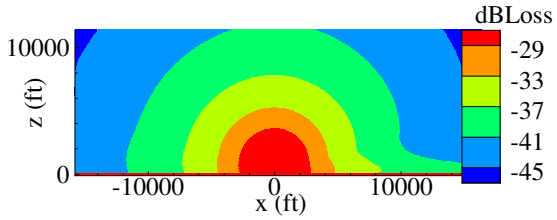

Figure 7: dB loss on the xz plane with wind blowing from β =180°.

The second validation involves propagation in the presence of a crosswind. For this case, the same magnitude of wind speed was used as in the first validation effort, but is now changed to 27° off the nose (on the starboard side) of the vehicle ($\beta = 153°$), as shown in Figure 8. In this case, the elevation contours still expand in the $\psi = \beta$ direction and contract in the $\psi = \beta + 180°$ direction. It is as if Figure 6a is rotated by angle, β. This rotation is shown in Figure 8 for $\beta = 153°$ using both WC and ray computations, which agree well with each other. If the gradients are stronger, these effects become significant at shorter distances. It is important to note that at distances within 2000 ft of the source, the elevation and azimuth angles are not significantly affected. This validates that source noise hemispheres created from near microphone measurements are not subject to the strong wind and temperature gradients used here.

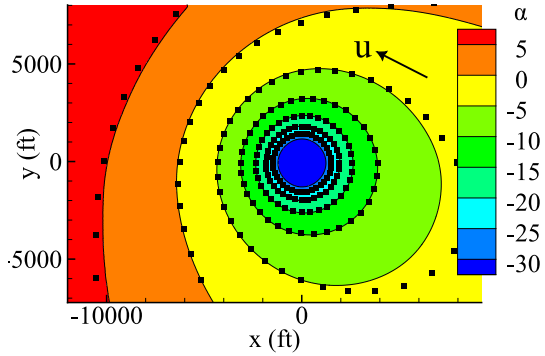

Figure 8: Elevation angles computed using WC (in color) compared with ray tracing (filled squares) on the ground plane for wind blowing from $\beta = 153°$.

FLIGHT TEST COMPARISONS

With the effects of varying wind conditions established, an analysis of accurate flight test conditions will be conducted. The source hemispheres used presently are computed from an MD530 level flyover test using conventional methods (Ref. 10). Those hemispheres are then propagated using WC to predict the sound levels at the far field microphones, approximately 2 miles away.

Problem Set-up

Several flight conditions were executed over the duration of the flight test; however, in the present work, the analysis is restricted to a steady level flight condition. The target airspeed was 120 kts, and the target altitude was 200 ft. The flight path was chosen to take the vehicle through the center of a symmetric ground-based microphone array. This flight condition was repeated a total of eight times over two separate days, two of which were selected for this study. Flights began at first light and were typically completed by mid morning to take advantage of the calmer winds. The test runs and aircraft (source) positions used for comparison are shown in Table 1.

An extensive set of weather measurements were collected throughout the test, including temperature and wind profiles. Atmospheric temperature variation was recorded from ground

Table 1: Aircraft locations for runs 038403 and 042420.

Run #	x_s [ft]	y_s [ft]	z_s [ft]
038403	-8451	-147	147
042420	-8331	-148	163

level to approximately 500 ft altitude using a tethered weather balloon and temperature sonde with sensors every 10 ft and accuracy of ± 0.07 °C. Wind velocity as a function of altitude was measured with a LIDAR system for 12 altitudes between ground level and 1000 ft.

The physical domain for the computations is 14000 ft $\times$ 5792 ft $\times$ 2848 ft in x, y, z directions, respectively, as shown in Figure 9. Since the test site is approximately flat, a ground

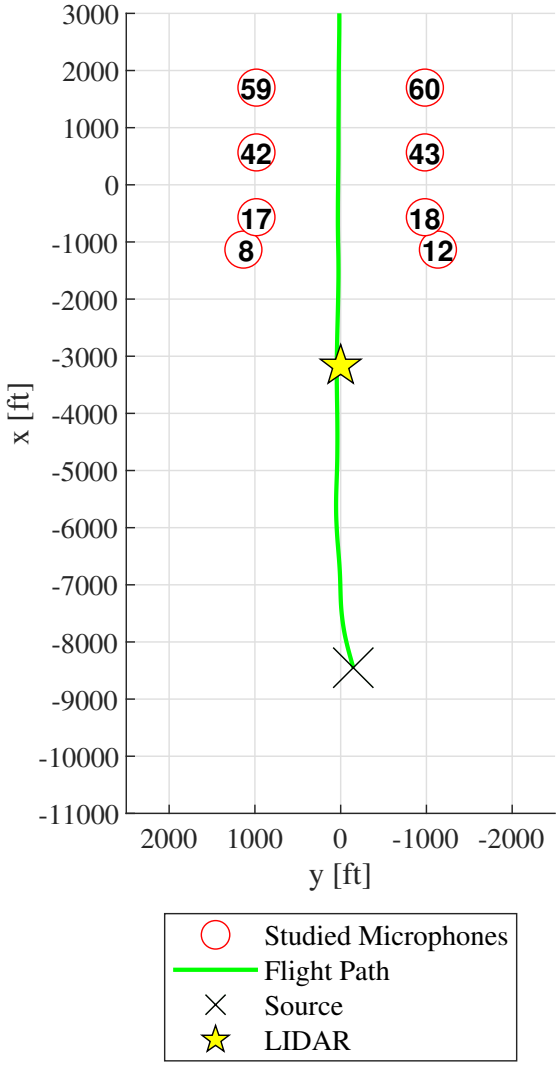

Figure 9: Computational domain with studied microphones and source location for run 038403.

boundary condition at $z = z_{reference} = 0$ is included, which involves an immersed boundary, where $\phi_k = 0$, at $z < 0$. This is discussed in more detail in Ref. 30. A uniform grid with grid cell size of 8 ft is used for all the flight test comparisons shown in this paper, resulting in the grid size of 1750 $\times$ 724 $\times$ 356 in the x, y and z directions, respectively.

The measured temperature and wind data are fitted to the grid in the z direction, assuming no variation in other directions. Wind speed and speed of sound (calculated using the curve-fitted temperature data) are shown in Figures 10 and 11, respectively, for runs 038403 and 042420. Even though the

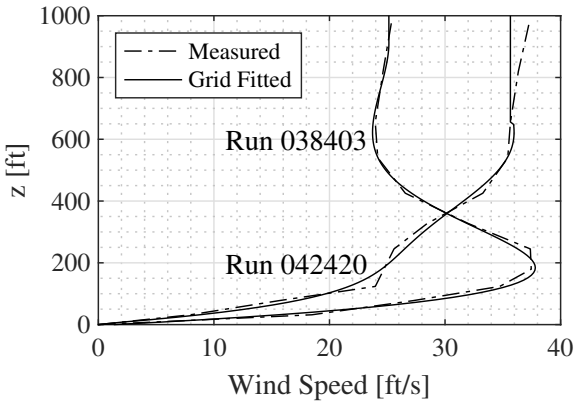

Figure 10: Wind speed vs height for runs 038403 and 042420. Comparison of measured data (dashed lines) and curve-fitted data (solid line).

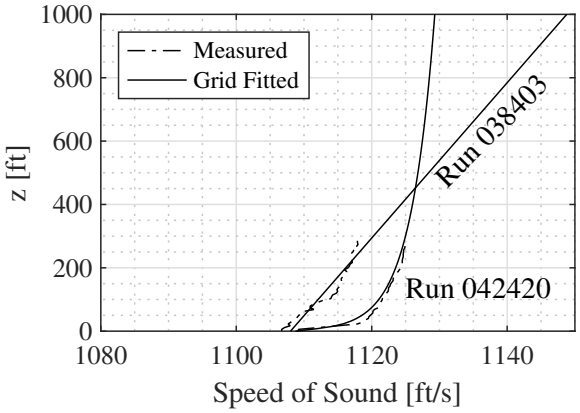

Figure 11: Speed of sound vs height for runs 038403 and 042420. Comparison of measured data (dashed lines) and curve-fitted data (solid line).

measured wind direction varies in z, an average direction is used everywhere for the computations. Since it is impossible to exactly measure the transient atmosphere, using an approximation is reasonable. Average wind directions for tests 038403 and 042420 are 153° and 164°, respectively. This means that in both cases the wind is predominantly a head-wind coming from slightly to the pilot's right. The computational wave is then propagated from the source location, across the entire domain, through these weather conditions, and all integrals are calculated at each point of interest.

Source Sphere Interpolation

Emission angles $(\psi_{emit}, \theta_{emit})$ computed using WC are then used to find the source spectra at the microphones shown in Figure 9. The coordinates of these microphones are shown in the Table 2. The microphones chosen for comparison are on both advancing and retreating sides and at varying distances, which will provide a wider range for the study. Microphones 12, 18, 43, and 60 are on the advancing side, while microphones 8, 17, 42, and 59 are on the retreating side. The z coordinates for all these microphones are within ± 8 ft, which is the grid cell size used for the comparisons. Therefore, they are adjusted to $z = 0$ to be consistent with the flat ground.

Table 2: Coordinates for microphones used for comparisons.

Mic #	x [ft]	y [ft]	z [ft]	$z_{adjusted}$ [ft]
8	-1120	1133	-4	0
12	-1127	-1140	9	0
17	-555	981	-4	0
18	-566	-982	6	0
42	577	992	-5	0
43	576	-974	5	0
59	1706	977	-5	0
60	1705	-984	4	0

The calculated acoustic emission angles $(\psi_{emit},\ \alpha_{emit})$ do not necessarily align with measured spectral locations on the source hemisphere. In such cases, the initial spectra at these coordinates are estimated using an inverse distance weighting scheme, where contributions from any point on the hemispheres are weighted inversely to their geodesic distance from the computed point $(\psi_{emit},\ \alpha_{emit})$ (Ref. 32). Only points within a specified radius of interpolation are considered.

Let p_i^2 be the square of pressure at point, $(\psi_i,\ \alpha_i)$, on the source hemisphere, where i is the index of the grid point with a total of n grid points. The emission pressures at $(\psi_{emit}, \alpha_{emit})$ are then calculated as

$$p^2_{emit} = \sum_{i=1}^{n} w_i p_i^2, \tag{9}$$

where w_i is the inverse distance weighting factor calculated using,

$$w_i = \frac{m_i}{M}, \tag{10}$$

with

$$m_i = \left(\frac{r_{interp} - s_i}{r_{interp}\ s_i} \right)^2 \tag{11}$$

and

$$M = \sum_{i=1}^{n} m_i. \tag{12}$$

Here r_{interp} is the radius of interpolation and s_i is the geodesic distance between $(\psi_{emit},\ \alpha_{emit})$ and $(\psi_i,\ \alpha_i)$. For this work, $r_{interp} = 30^\circ$ was used. It was found that varying this value between 10° and 40° had negligible impact on the resulting spectra (order 1/100 dB at first harmonic). The interpolated p^2_{emit} is then converted back to decibels, dB_{emit}. This is repeated for every emitted acoustic signal.

Due to the atmospheric conditions, it was found that the acoustic signal received at all microphones during the run 038403, originated at positive elevation angles (above the rotor plane), for which the source hemisphere cannot provide data. In this case, the inverse weighting interpolation scheme was still successfully applied, from a mathematical standpoint at least: the algorithm simply selected the data points on the hemisphere that were within r_{interp}. It should be noted that this interpolation and extrapolation scheme is employed without regard to potential differences in aerodynamic condition above the rotor plane, and so results are not ideal.

Far-Field Spectra

Using the source spectra, dB_{emit}, corresponding to each microphone in Table 2, final sound spectra are calculated. First, attenuation factor, A_f and arrival time, τ, are adjusted to the radius of the source hemisphere, R, which is different from the initial radius of the computational wave, R_{cw}. This is done using the relations,

$$A_{emit} = \frac{A_f\ R_{cw}}{R} \tag{13}$$

and

$$\tau_{emit} = \tau + (R - R_{cw})/c_{avg}, \tag{14}$$

where c_{avg} is the average speed of sound. For the cases shown in this paper, $R = 100$ ft. The final spectra are then calculated as

$$\begin{aligned} dB_{final}(\omega + \omega_{\text{dopp}}) = \\ dB_{emit}(\omega) \\ + 20\ \log_{10}(A_{emi}) \\ - \text{dBLoss}_{atm}(\omega)\ l, \end{aligned} \tag{15}$$

where ω is the frequency in Hz, ω_{dopp} is the shift in frequency due to Doppler effect, dBLoss_{atm} is loss due to atmospheric absorption and l is the path length calculated using the average speed of sound. Since the speed of sound variations are within 5% for most of the cases, this is a reasonable choice.

RESULTS AND DISCUSSION

Wind and temperature gradients, together, can increase or decrease the combined refractive index depending on their gradient and the angle between azimuth and wind directions. Therefore, the effective speed of sound, c_e, is equal to sum of speed of sound and wind speed in the direction of the wave. This can be written as

$$c_e(z) = c_\psi(z) + u_\psi(z), \tag{16}$$

where u_ψ is the component of wind along the azimuthal direction, which is not same as $\vec{u}$ used for WC computation.

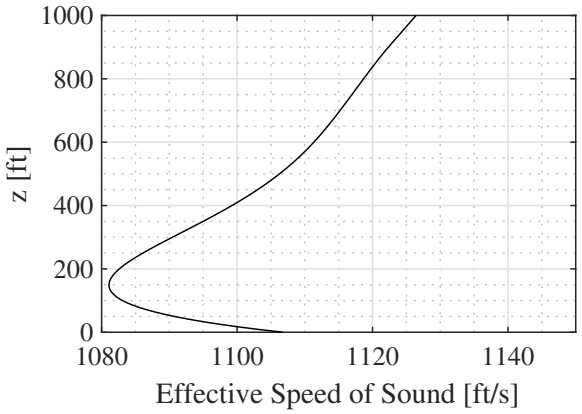

Figure 12: Effective speed of sound for run 038403 as a function of height.

Atmospheric Ducting Case

Run 038403 is the first condition investigated. For this case, c_e is shown in Figure 12 at $\psi = 180°$. Here, the effective speed of sound shows a strong decreasing gradient at altitudes below 150 ft, followed promptly by an increasing gradient above that altitude. This condition results in a very unique propagation environment, as will be seen.

A qualitative detail of the propagation due to the effective speed of sound for run 038403 is computed using ray tracing on $\psi = 180°$ and is shown in Figure 13. It can be seen

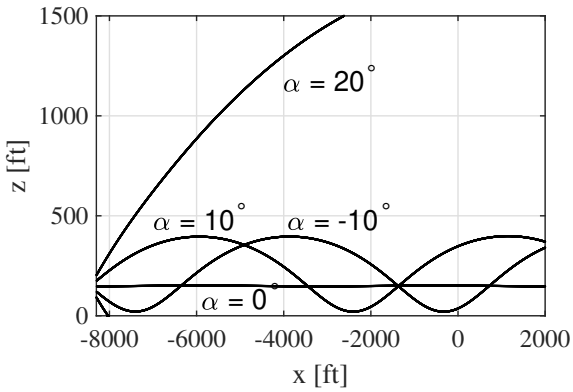

Figure 13: Direct wave propagation on $\psi = 180°$ plane computed using ray tracing. Wave "hopping" is due to refraction above the ground. Reflected rays are not plotted.

that there is a significant downward bending as expected due to increasing speed of sound. At elevation angles above the horizon ($\alpha > 0°$), rays bend downward first, due to increasing speed of sound. When they enter the region with decreasing speed of sound, they slowly turn around and bend upward. Similarly, when the elevation angle is below the horizon ($\alpha < 0°$), the rays initially bend upward, then are curved downward when the speed of sound begins to increase. This process repeats, causing multiple wave hops, and is a classic example of a waveguide or atmospheric ducting. This phenomenon is observed due to the speed of sound profile formed from the combination of wind and temperature gradients.

The "hops" shown in Figure 13 are due to refraction of the direct wave and happen above the ground. At $\alpha = 0°$, the ray travels straight since the source height was coincidentally equal to the altitude of the minimum effective speed of sound ($z_s = 147$ ft). If the source was above that height, the ray at $\alpha = 0°$ would have refracted downward first. Reflected waves observed at angles below $\alpha = -10°$ are not shown in Figure 13, but they will also exhibit similar behavior. It is important to note that because the waves from above the hemisphere also reach the ground, there may be errors in source spectra calculation.

For a more detailed study, comparisons of sound spectra at select microphone locations are shown in Figure 14. Measured data are extracted using the the arrival time, τ_{emit}, and are compared to the propagated amplitudes from the source sphere. The measured spectral levels are averaged between the three nearest timestamps to the arrival time (total of 1.5s of averaging), in order to decrease the variability present in the measured spectra. Doppler effects are not included in both the measured and computed spectra, to maintain consistency.

Broadly speaking, for run 038403, there is a good agreement among the measurements and the propagated spectra calculated by Wave Confinement and straight ray propagation. Peaks at main rotor harmonics (multiples of ~40 Hz) and tail rotor harmonics (multiples of ~95 Hz) are noticeable. The peak values appear to match well among the three conditions shown for all 8 microphones. There are some discrepancies, that will be investigated further.

Microphone 8 is approximately 7300 ft ahead of the source with an elevation emission angle (α_{emit}) of 3°, which is outside the source hemisphere. Since it is not that far from the $\alpha = 0°$ plane, the computed spectrum shown in Figure 14a matches well with the measured data. Microphone 17, which is ~ 7900 ft ahead of the source with $\alpha_{emit} = 3.75°$, also has an excellent match with measured data. The predicted data are within 6 dB of the measured data at all frequencies of interest for this microphone.

Microphone 42, which is ~ 9000 ft from the source, has a higher emission elevation angle of 5.4°, which affects the predicted data more significantly. Main rotor harmonics have an overprediction of less than 6 dB at the first four harmonics, while higher tail rotor harmonics have up to 12 dB overprediction. Microphone 59, shown in Figure 14g is about 10,000 ft away, and has an emission elevation angle of about 7 degrees, which is far above the $\alpha = 0°$ plane. Despite this, spectra at microphone 59 agree fairly well with the measured data with all harmonics within 12 dB for both WC and straight ray propagation.

Similar results can be observed for advancing side microphones, 12, 18, 43, and 60, with a slight increase in deviation between measured and propagated signals. It is easier to investigate potential spectral differences using Figure 15, which portrays the difference between the propagation methods and the measured spectra, at discrete main and tail rotor frequencies. The first four main rotor blade passage frequencies (40, 80, 120, 160 Hz) were selected, along with the first six tail

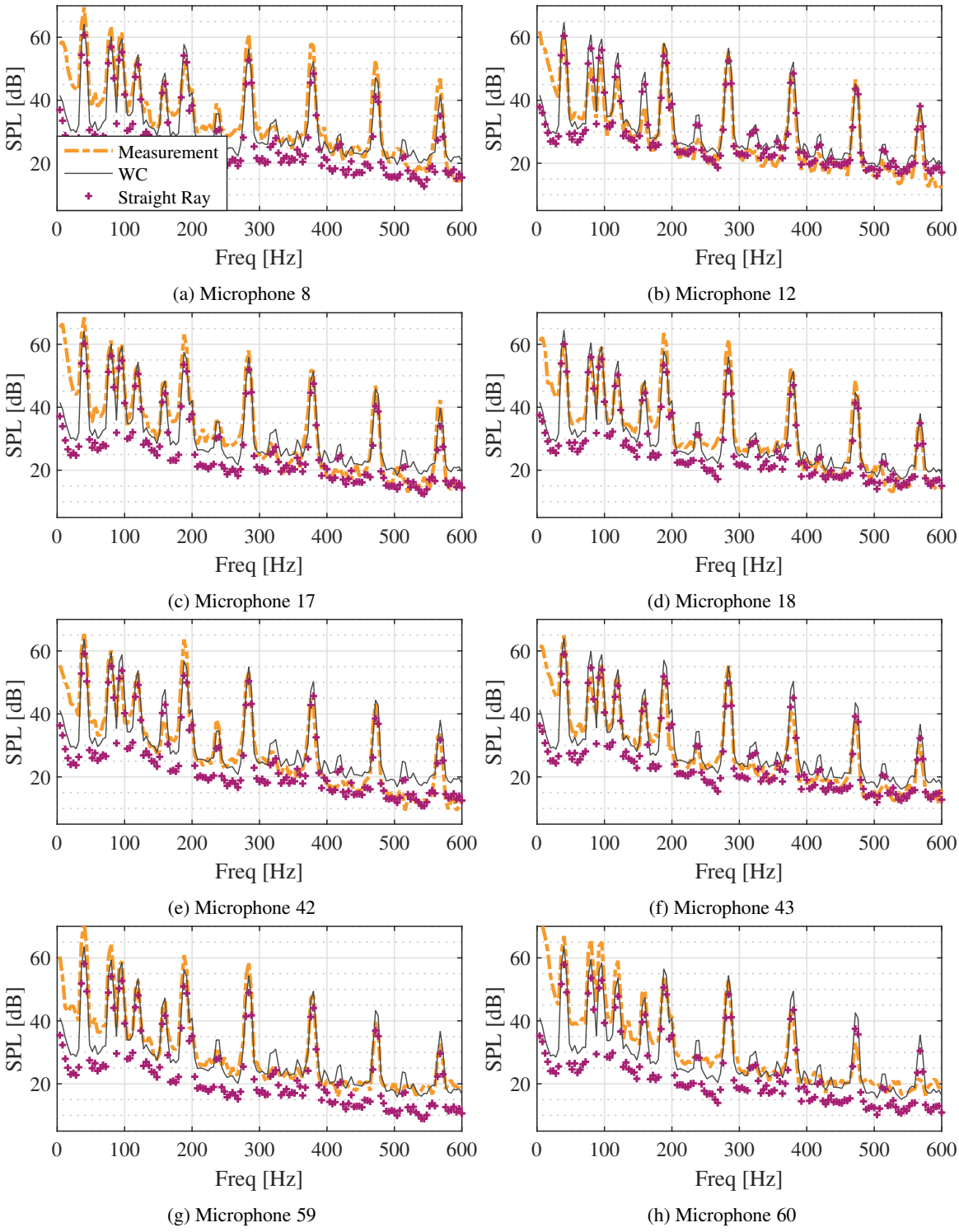

(a) Microphone 8

(b) Microphone 12

(c) Microphone 17

(d) Microphone 18

(e) Microphone 42

(f) Microphone 43

(g) Microphone 59

(h) Microphone 60

Figure 14: Sound Spectra for run 038403 using measured test data (orange dashed line), WC (dark solid line), and a straight ray calculation ('+' symbol).

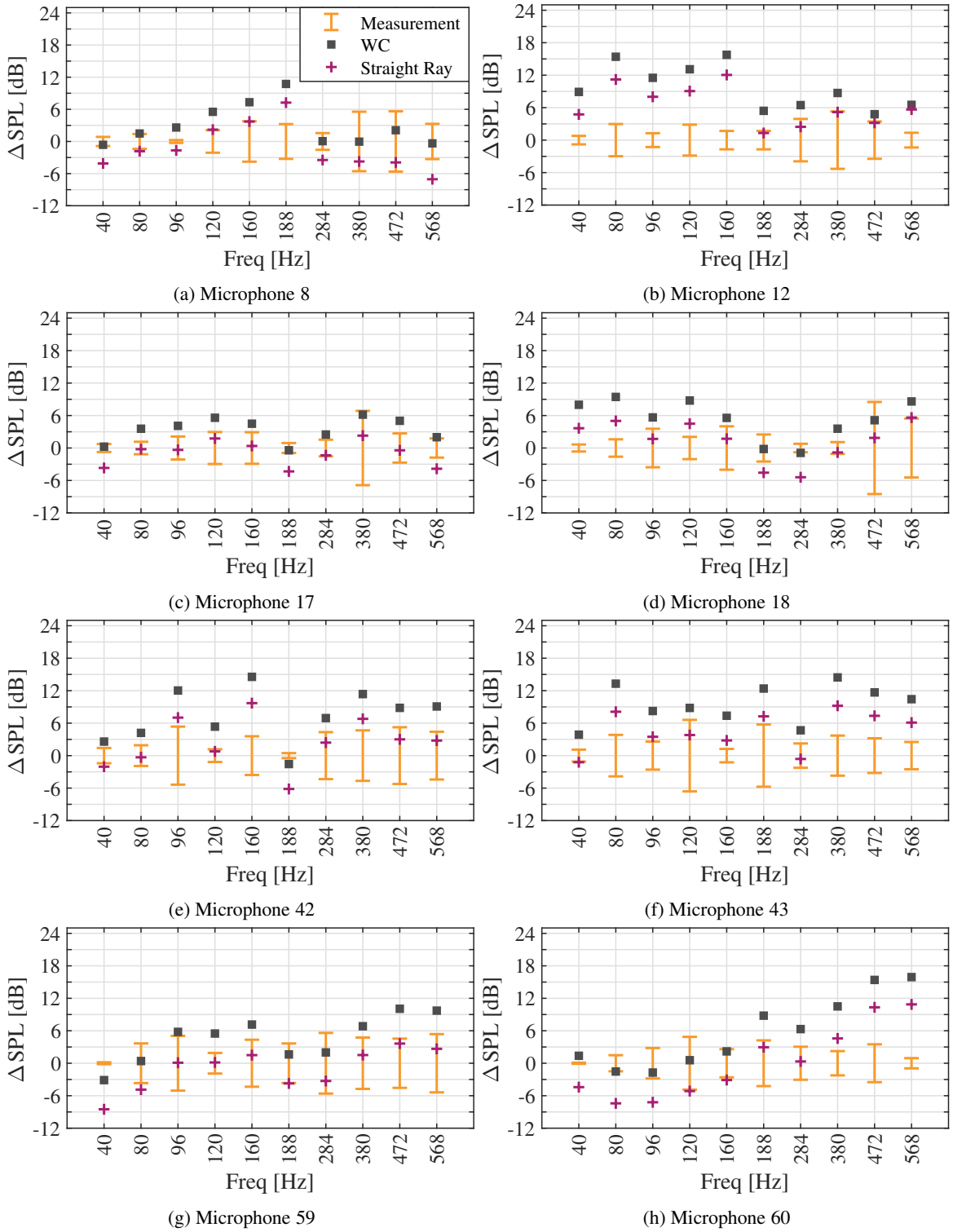

(a) Microphone 8

(b) Microphone 12

(c) Microphone 17

(d) Microphone 18

(e) Microphone 42

(f) Microphone 43

(g) Microphone 59

(h) Microphone 60

Figure 15: Sound pressure level difference for run 038403 between WC (square), straight ray ('+'), and the measurement value at select frequencies. Standard deviation for 3 spectra nearest the arrival time are provided to show measurement variability.

rotor blade passage frequencies (96, 188, 284, 380, 472, 568 Hz). The frequencies chosen are based on their amplitude peaks shown in Figure 14, and are matched to the 4 Hz bin-width of the measurement spectra. The standard deviation of each measured harmonic for the 1.5 s of data that comprised the average spectra seen in Figure 14 are also portrayed here.

It can be seen in Figure 15 that the WC prediction for each amplitude is variable, but approximately 6 dB higher than the straight ray amplitude. This is, as expected, due to downward refraction shown in Figure 13, caused by the varying atmosphere, which cannot be accounted for by the straight ray method.

Overall, the main rotor harmonics tend to match better than the tail rotor harmonics. The main rotor acoustic emissions at the source are less susceptible to variation in winds than the tail rotor, and so this result is encouraging. The tail rotor associated noise, however, is quite variable between microphones and is highly susceptible to crosswinds. Also, source spectra used for both WC and straight ray propagation models are quite similar, despite a significant difference in their atmospheres, causing significantly different α_{emit}. This is because of lack of information above the hemisphere, and hence, it is strongly suspected that the source hemisphere is the item in error. Another factor that effects the source hemisphere is that it comes from the linear array and is measured at least 7,000 ft (approximately 35 s of flight time) further into the flight than the source location used at emission. During the time between propagation location and hemisphere measurement location, the winds and other flight conditions could have changed. The standard deviations shown in Figure 15 are from the three 0.5 s spectral values nearest to the WC predicted arrival time. These relatively large standard deviations hint at the large variability seen in a short period of time, let alone across 35 s.

It is also important to note here that there are multiple ground reflections as well, due to atmospheric ducting. This will impact the results shown since reflections (more specifically, ground impedance effects) are not accounted for in the present modeling effort. This is another potential cause for the discrepancy between model and measured data seen in Figures 14 and 15.

Benign Atmosphere

A second condition is investigated here that has a more typical weather profile. For run 042420, the effective speed of sound is shown in Figure 16 at $\psi = 180$. Speed of sound is slowly decreasing over most of the height, causing the rays at angles above -6° to refract upward before they reach the ground. At angles below -6°, the rays reflect from the ground and continue upward (which are not show in Figure 17). An envelope of these refracted rays also focus at a region, 150 ft height above ground in the shape of a caustic curve. It is well-known that ray tracing fails in these regions. Additionally, ray tracing needs very high resolution between -7° and -8° to capture all the rays that reach the ground. If ray tracing was used to to simulate the propagation, as seen in Figure

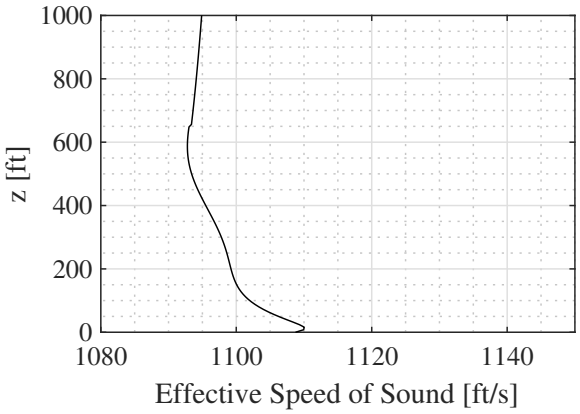

Figure 16: Effective speed of sound for run 042420 as a function of height.

17, a shadow region is formed in front of the source, preventing any sound from reaching that area. This is not the case in reality, where sound from the caustic region also reaches the ground. Since WC directly solves the wave equation, which intrinsically includes all the propagation effects, these regions are automatically captured without using extra equations.

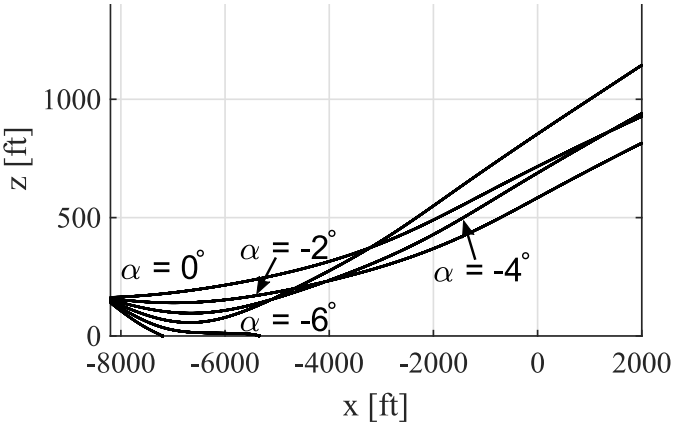

Figure 17: Direct wave propagation on $\psi = 180°$ plane computed using ray tracing.

All measured and computed spectra for this condition and the selected microphones are shown in Figure 18. Similar to Figure 15, the difference between propagated and measured values are shown in Figure 19. Here, the sound signals propagated by WC are approximately 3 dB smaller than the straight ray propagation values due to upward refraction (or increasing ray tube diameter) and sound propagation from the caustics region. Overall, however, there is an excellent agreement for all microphones.

There are some notable examples where the predicted values do not match the measured data, such as microphone 60 (Figure 19h). There, however, both the straight ray and WC methods agree, suggesting the error lies in the source emission definition used, and not the propagation methods.

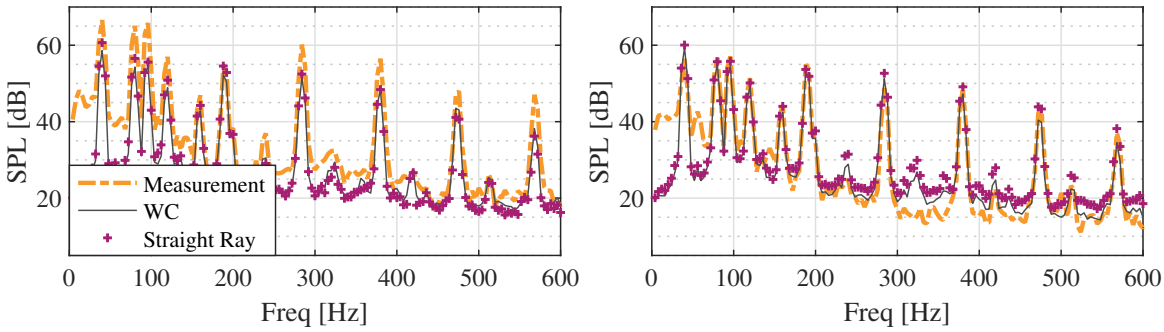

(a) Microphone 8

(b) Microphone 12

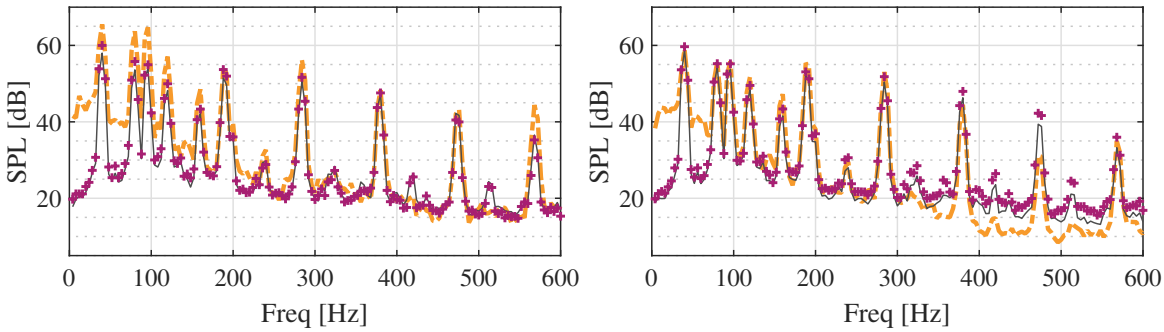

(c) Microphone 17

(d) Microphone 18

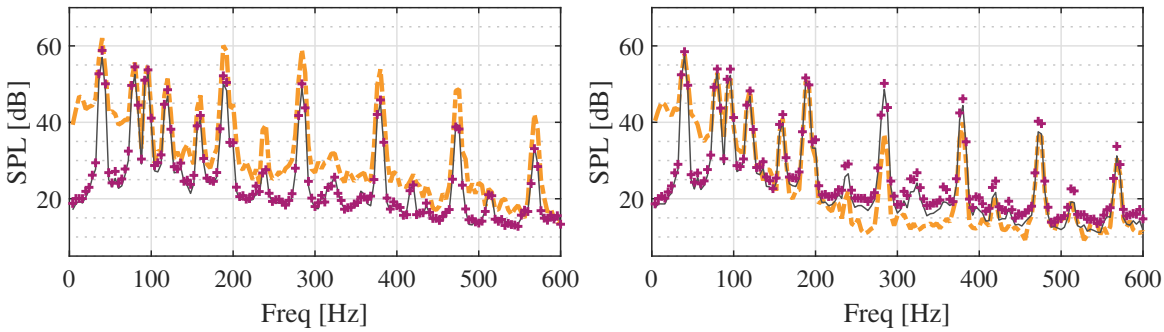

(e) Microphone 42

(f) Microphone 43

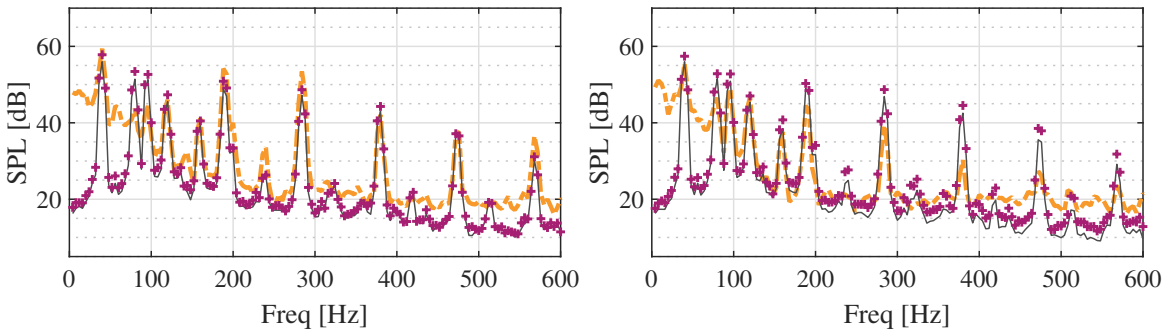

(g) Microphone 59

(h) Microphone 60

Figure 18: Sound Spectra for run 042420 using measured test data (orange dashed line), WC (solid line), and straight ray ('+').

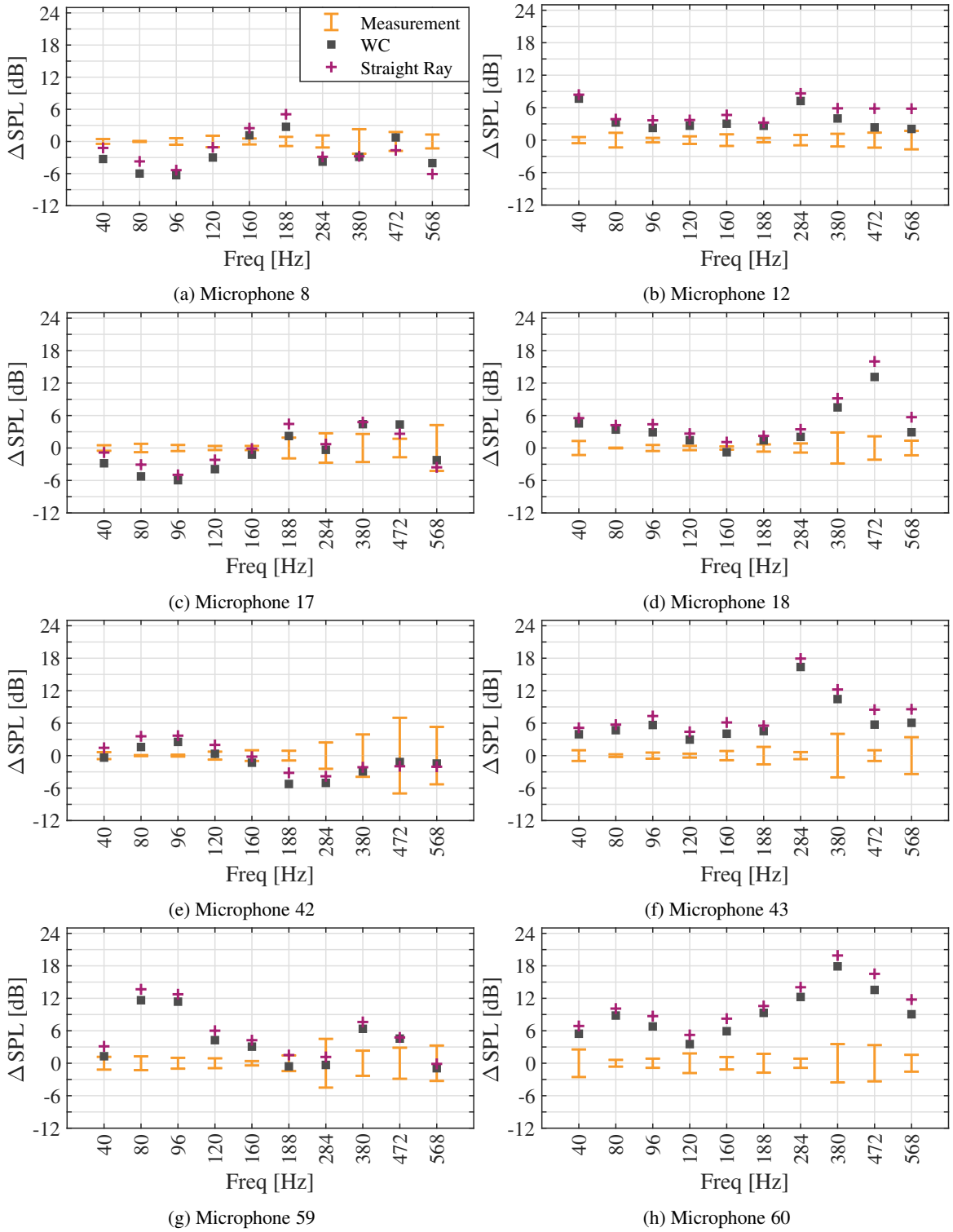

(a) Microphone 8

(b) Microphone 12

(c) Microphone 17

(d) Microphone 18

(e) Microphone 42

(f) Microphone 43

(g) Microphone 59

(h) Microphone 60

Figure 19: Sound pressure level difference for run 042420 between WC (square), straight ray ('+'), and the measurement value at select frequencies. Standard deviation for 3 spectra nearest the arrival time are provided to show measurement variability.

CONCLUDING REMARKS

In this paper, Wave Confinement is used to simulate long distance propagation of rotorcraft noise through various adverse atmospheric conditions. One of the advantages of WC is that it does not incur numerical dissipation errors despite the use of coarse grids since the physical waveforms (which are usually shorter than a grid cell) are not directly propagated on the grid, but the details are carried by computational waves that span over a few grid cells. These computational waves can also accurately capture propagation effects due to temperature and wind gradients and reconstruct physical waveforms in the far field.

Validations for propagation through wind at different angles show that WC can accurately capture deviations in emission angles. For wind speeds used in this paper, there is no noticeable deviation in the azimuth angle, which is also demonstrated using both WC and ray tracing. The WC method also compares quite favorably to measured acoustic emissions of rotorcraft vehicles even under adverse weather conditions experienced during the Yuma, AZ flight test. One observation is that crosswind conditions can significantly impact the tail rotor source amplitudes, which has a detrimental effect when comparing long range propagation values. Also, effective speed of sound due to wind and temperature gradients can realistically create atmospheric duct-like regions near the ground that can cause acoustic waves from above the source hemisphere to reach the ground.

ACKNOWLEDGMENTS

We acknowledge the U.S. Army SBIR program for funding this work under contract #W911W6-12C-0024. We also acknowledge Dr. Frank Caradonna for his valuable suggestions and insights, which helped in the successful development of the Wave Confinement method.

REFERENCES

1. Fryer, G. J. and Frazer, L. N., "Seismic waves in stratified anisotropic media," *Geophysical Journal International*, Vol. 78, (3), 1984, pp. 691–710.

2. Wait, J. R., Cullen, A. L., Fock, V., Wait, J. R., and Hagger, H. J., *Electromagnetic Waves in Stratified Media*, Elsevier, 1996.

3. Vail, E., "Adopt Local Law- Amending Chapter 75 (Airport) of the Town Code Regulating Nighttime Operation of Aircraft at East Hampton Airport," East Hampton Town Board Resolution 2015-411, 2015.

4. Uber, "Fast-Forwarding to a Future of On-Demand Urban Air Transportation," *White Paper*, 2016.

5. Vertical Flight Society, "Vertical Flight Society Electric VTOL Directory Hits 600 Concepts," *Press Release*, January 2022.

6. Pascioni, K. A., Watts, M. E., Houston, M. L., Lind, A. H., Stephenson, J. H., and Bain, J. J., "Acoustic Flight Test of the Joby Aviation Advanced Air Mobility Prototype Vehicle," *28th AIAA/CEAS Aeroacoustics Conference*, 2022.

7. Noise Standards: Aircraft Type and Airworthiness Certification, Code of Federal Regulations, Title 14, Chapter 1, Part 36, Appendix H.

8. Conner, D. A. and Page, J. A., "A tool for low noise procedures design and community noise impact assessment: The Rotorcraft Noise Model (RNM)," AHS International Technical Specialists"Meeting on Advanced Rotorcraft Technology and Life Saving Activities, Tochigi-ken, Japan, November 2002.

9. Steinhoff, J. and Chitta, S., "Solution of the Scalar Wave Equation over Very Long Distances Using Nonlinear Solitary Waves: Relation to Finite Difference Methods," *J. Comput. Phys.*, Vol. 231, (19), 2012, pp. 6306–6322.

10. Page, J. A., Plotkin, K. J., and Hobbs, C., "Acoustic Repropagation Technique Version 2 (ART2)," *Wyle Laboratories. Arlington: Wyle Laboratories*, 2001.

11. "Ground-Plane Microphone Configuration for Propeller-Driven Light-Aircraft Noise Measurement," ARP 4055, SAE, November 2007.

12. Stephenson, J. H. and Houston, M., "Evaluation of Acoustic Snapshot Arrays for Rotorcraft Source Noise Characterization," Proceedings of the 48th European Rotorcraft Forum, Winterthur, Switzerland, September 2022.

13. Stephenson, J. H., Lind, A., Hutchins, C., Pascioni, K., Houston, M., and Martin, P., "Yuma 2022 Rotorcraft Acoustic Flight Test," Technical Memorandum NASA/TM-20220004483, NASA Langley Research Center, Hampton, VA 23681, USA, April 2022.

14. Greenwood, E. and Schmitz, F. H., "Separation of Main and Tail Rotor Noise from Ground-Based Acoustic Measurements," *Journal of Aircraft*, Vol. 51, (2), March 2014, pp. 464–472.

15. Stephenson, J. H., Sim, B. W., Chitta, S., and Steinhoff, J., "Sound Diffraction Modeling of Rotorcraft Noise Around Terrain," Proceedings of the 73rd Annual Forum of the American Helicopter Society, Ft. Worth, TX, May 2017.

16. Attenborough, K., Taherzadeh, S., Bass, H. E., Di, X., Raspet, R., Becker, G. R., Güdesen, A. D., Chrestman, A. M., Daigle, G. A., L'esperance, A., Gabillet, Y., Gilbert, K. E., Li, Y. L., White, M. J., Naz, P., Noble, J. M., and van Hoof, H., "Benchmark cases for outdoor sound propagation models," *Journal of the Acoustical Society of America*, Vol. 97, 1995, pp. 173–191.

17. Bass, H. E., Sutherland, L. C., Zuckerwar, A. J., Blackstock, D. T., and Hester, D. M., "Atmospheric absorption of sound: Further developments," *Journal of the Acoustical Society of America*, Vol. 97, 1995, pp. 680–683.

18. Pierce, A., *Acoustics: An Introduction to Its Physical Principles and Applications*, Vol. 34, June 1989. doi: 10.1063/1.2914388

19. Anderson, M. C., Stephenson, J. H., Zawodny, N. S., and Gee, K. L., "Characterizing the effects of two ground-based outdoor microphone configurations," Proceedings of Meetings on Acoustics 178ASA, Vol. 39, 2019.

20. Ostashev, V. E., Wilson, D. K., Liu, L., Aldridge, D. F., Symons, N. P., and Marlin, D., "Equations for finite-difference, time-domain simulation of sound propagation in moving inhomogeneous media and numerical implementation," *The Journal of the Acoustical Society of America*, Vol. 117, (2), 2005, pp. 503–517.

21. Wilson, D. K. and Liu, L., "Finite-Difference, Time-Domain Simulation of Sound Propagation in a Dynamic Atmosphere," Technical Report ADA423222, Cold Regions Research and Engineering Lab, Hanover, NH, 2004.

22. Renterghem, T. V., "Efficient Outdoor Sound Propagation Modeling with the Finite-Difference Time-Domain (FDTD) Method: A Review," *International Journal of Aeroacoustics*, Vol. 13, (5-6), 2014, pp. 385–404.

23. Salomons, E. M., *Computational Atmospheric Acoustics*, Springer Dordrecht, 2001.

24. Cheng, R., Morris, P. J., and Brentner, K. S., "A 3D Parabolic Equation Method for Wind Turbine Noise Propagation in Moving Inhomogeneous Atmosphere," *12th AIAA/CEAS Aeroacoustics Conference*, 2006.

25. West, M., Gilbert, K., and Sack, R., "A tutorial on the parabolic equation (PE) model used for long range sound propagation in the atmosphere," *Applied Acoustics*, Vol. 37, (1), 1992, pp. 31–49.

26. Oliveira, A. P., *The effect of wind and turbulence on sound propagation in the atmosphere*, Ph.D. thesis, Technical University of Lisbon, 2012.

27. Salomons, E. M., "Improved Green's function parabolic equation method for atmospheric sound propagation," *The Journal of the Acoustical Society of America*, Vol. 104, (1), 1998.

28. Vinje, V., Iversen, E., and Gjoystdal, H., "Traveltime and amplitude estimation using wavefront construction," *Geophysics*, Vol. 58, (8), 1993, pp. 1157–1166.

29. Ionescu, D.-C. and Igel, H., "Transparent Boundary Conditions for Wave Propagation on Unbounded Domains," Computational Science,ICCS 2003, edited by P. M. A. Sloot, D. Abramson, A. V. Bogdanov, Y. E. Gorbachev, J. J. Dongarra, and A. Y. Zomaya, 2003.

30. Chitta, S., Steinhoff, J., Wilson, A., Caradonna, F., Sim, B., and Sankar, L., "A New Finite-Difference Method for General Long-Range Rotorcraft Acoustics: Initial Comparisons with Intermediate-Range Data," *American Helicopter Society 70th Annual Forum*, 2014.

31. Ostashev, V. E. and Norris, D., "Ray tracing in a stratified moving atmosphere: Azimuthal deviation in sound propagation," *The Journal of the Acoustical Society of America*, Vol. 151, (1), 2022, pp. 451–456.

32. Shepard, D., "A two-dimensional interpolation function for irregularly-spaced data," Proceedings of the 1968 23rd ACM national conference, 1968.